ES Materials & Manufacturing

RESEARCH PAPER View Article Online

# Ultrathin $MoSe_2$ Nanosheets Coated on Hollow Carbon Spheres as Efficient Hybrid Catalyst for Hydrogen Evolution Reaction

Qin Yuan,[1] Ruijing Wang,[1] Qunlong Wang,[2] Peng Sun,[1] Rongrong Nie[1] and Xuefeng Wang[1*]

Two-dimensional transition metal chalcogenide is a promising non-precious metal electrocatalyst for hydrogen evolution reaction (HER); however, the improvement of an inefficient catalytic activity is still a major challenge at present due to their limited active sites and low conductivity. In this work, we present ultrathin $MoSe_2$ nanosheets were coated on hollow carbon spheres (HCS) surface through strong interaction with surface hydrophilic functional groups OH to fabricate a core-shell HCS@$MoSe_2$ hybrid catalyst. The $MoSe_2$ structure with nanosheets could effectively expose more active edges and the HCS core further provides a beneficial conductivity. Finally, the obtained composite shows the remarkable HER activity with a small Tafel slope of 74 mV $dec^{-1}$, a small overpotential of 200 mV at a current density of 10 mA $cm^{-2}$, and an excellent long-term durability. Therefore, this Pt-free and highly efficient electrocatalyst shows its great potential for renewable hydrogen production.

**Keywords:** Molybdenum diselide; Hollow carbon spheres; Hydrogen evolution reaction

**Received** 3 December 2018, **Accepted** 13 December 2018

**DOI:** 10.30919/esmm5f112

## 1. Introduction

Transition metal chalcogenides (TMDs), composed of covalently bonded X-M-X (M= Mo, W; X= S, Se, Te) layers by van der waals forces, have received much attention in energy conversion and storage fields due to their tunable band structure and intrinsic electrochemical properties.[1-2] Among them, $MoS_2$ and its hybrids are the most popular electrocatalytic materials that have been widely investigated for the hydrogen evolution reaction (HER).[3-6] The $MoSe_2$ materials, which have the similar electronic structure and physicochemical properties as $MoS_2$, have gradually attracted the general interest.[7-8] However, bulk $MoSe_2$ is a poor catalyst for HER because of limited catalytic active sites.[9] Recent works focus on increasing the $MoSe_2$ active sites and improving its conductivity,[10-12] and several strategies were demonstrated to enhance intrinsic HER catalytic activity. For example, Lai et al. used bacterial cellulose-derived carbon nanofibers to assist the uniform growth of few-layered $MoSe_2$ nanosheets (CBC/$MoSe_2$), which effectively increased the active sites and conductivity of $MoSe_2$ for HER.[13] Wang et al. prepared $MoSe_2$ on a reduced grapheme oxide (rGO)/polyimide (PI) composite substrate by electrochemical deposition, which showed superior catalytic acitivity in HER.[14] Deng et al synthesized N-$MoSe_2$/VG shell/core arrays that remarkably boost their HER activity by means of the improved conductivity and rich catalytic active sites.[15]

[1]*Shanghai Key Lab of Chemical Assessment and Sustainability, School of Chemical Science and Engineering, Tongji University, Shanghai 200092, China*

[2]*Shanghai Joyworld Innovative Materials Technology Co. LTD, Shanghai 200433, China*

***E-mail:** xfwang@tongji.edu.cn*

These composites of $MoSe_2$ are assembled onto the conductive carbon matrix. Recently hollow carbon spheres have been demonstrated to be an attractive carbon materials morphology in ion batteries and supercapacitor, since the unique hollow structure could offer a large surface area and minimize the diffusion distances of electrolyte ions.[16-19] For example, hierarchical $MoS_2$ shell supported on carbon spheres as an anode material for LIBs manifest high specific capacity and good rate capability.[20]

In this study, we successfully prepared a composite with the hollow carbon spheres as a core and uniform $MoSe_2$ nanosheets as shell (denoted as HCS@$MoSe_2$). Encouragingly, this unique composite with ultrathin $MoSe_2$ nanosheets uniformly grown on HCS exhibits excellent catalytic activity for HER with a small overpotential and Tafel slope because the ultrathin $MoSe_2$ nanosheets covered the whole surface of HCS through strong interaction without obvious agglomeration, and the HCS core with a high conductivity compensates the low electron transfer of the TMDs.

## 2. Experimental

### 2.1. Chemicals

Absolute ethanol, NaOH (99 %), formaldehyde (37 wt%), ammonia solution (25 wt%), $Na_2MoO_4$ (99.0 %), selenium (99.9 %), hydrazine hydrate ($N_2H_4H_2O$, 80 wt%) solution, resorcinol (99.5 %), ethylorthosilicat (98 %) were used without further purification. All chemicals were purchased from Sinopharm Chemical Reagent Co., Ltd.

### 2.2. Preparation of Hollow Carbon Spheres

Ammonia aqueous solution (3 mL, 25 wt%) was added to a mixture of 10 mL deionized water and 70 mL ethanol. After the solution was stirred for 30 minutes, 3.46 ml ethylorthosilicate (TEOS), 0.4 g resorcinol and 0.56 ml formaldehyde solution (37 wt%) were added to

the above solution and stirred for 24 h at room temperature to form the solid $SiO_2$@$SiO_2$ products. Secondly, the product was collected by centrifugation and washed with absolute ethanol and distilled water several times, and vacuum-dried. The solid samples were carbonized by heating at 700 ℃ for 2 h under argon gas flow in a tube furnace. Finally, the $SiO_2$ templates were removed by treating the material in 2M sodium hydroxide for several hours, then the final HCS were also obtained by centrifugation and washed with distilled water before dried in vacuum at 80 ℃ for 24 h.

### 2.3. Fabrication of HCS@$MoSe_2$

Hollow carbon spheres (0.1 g) were added to the mixed solution which included 20 ml distilled water and 30 ml ethanol. After ultrasonic dispersion for 1 h, $Na_2MoO_4$ (0.4188 g) was added to the solution. Separately, selenium powder (0.3158 g) was dissolved in 10 ml of hydrazine hydrate solution in air atmosphere. The mixture was continuously stirred until a red-colored solution was obtained, and then the hydrazine hydrate-Se solution was slowly dropped into 50 ml of $Na_2MoO_4$ mixture solution at room temperature with rigorously stirring. The mixture turned dark red and the ratio of selenium and molybdenum is 2:1. The as-prepared precursor solution was transferred into the autoclave, sealed, and then heated at 200 °C for 12 h in an electric oven. The autoclave was then naturally cooled down to room temperature. After that, the black products were filtered off and washed with DI water several times to remove the residuals and then dried at 60 °C overnight. For comparison, $MoSe_2$ nanosheets were prepared through the same method in the absence of hollow carbon spheres.

### 2.4. Characterization

The morphology, structure, and composition of the electrode materials were characterized by field emission scanning (FE-SEM; Hitachi S-4800, Japan) and transmission (TEM; JEOL, JEM-2100, Japan) electron microscopes. Powder X-ray diffraction (XRD) patterns of the as-prepared samples were recorded using a Bruker Focus D8 with Cu Ka radiation. Raman spectra were collected using a Renishaw Invia Raman microscope with a 514 nm laser under ambient conditions. FTIR spectra were recorded at 1 $cm^{-1}$ resolution on a Bruker Vertex 70V with 0.1 $cm^{-1}$ accuracy using a three-reflection attenuated total reflection (ATR) accessory with a ZnSe internal reflection element (Harrick Scientific Products) and X-ray photoelectron spectroscopy (XPS; AXIS Ultra DLD).

### 2.5. Electrochemical measurements

Electrochemical measurements were performed on a CHI 660D electrochemical workstation. All measurements were tested in 0.5 M $H_2SO_4$ using a traditional three-electrode system with a graphite rod counter electrode, $Hg/Hg_2Cl_2$ (in saturated KCl solution) reference electrode and glassy carbon working electrode of 0.5 cm in diameter. The sample (4 mg) was first ultrasonically dispersed in 0.4 ml of Nafion solution (5 wt%), afterwards, the suspension (~10 μL) was attached onto a glass carbon (GC) electrode as a working electrode (loading about 0.196 mg $cm^{-2}$) and the as-prepared catalyst coating was dried at room temperature for at least 0.5 h. Linear sweep voltammetry curves (LSV) were obtained at a sweep rate of 5 mV $s^{-1}$ from -0.34 V to 0.06 V (vs. RHE). The pure $MoSe_2$ and commercial 10 wt% Pt/C were tested in the way described above for comparison. Electrochemical impedance spectroscopy (EIS) measurements were collected from 100 kHz to 0.1 Hz with an amplitude of 5 mV at an overpotential of 250 mV, and the EIS data was fitted by the ZView software. In electrochemical analysis, all the potentials were related to reversible hydrogen electrode (RHE) according to equation:

$$E\ (RHE) = E\ (Hg/Hg_2Cl_2) + (0.242 + 0.059\ pH)\ V$$

where E(RHE) is the reversible hydrogen electrode potential, and $E(Hg/Hg_2Cl_2)$ is the obtained potential versus saturated calomel electrode potential.

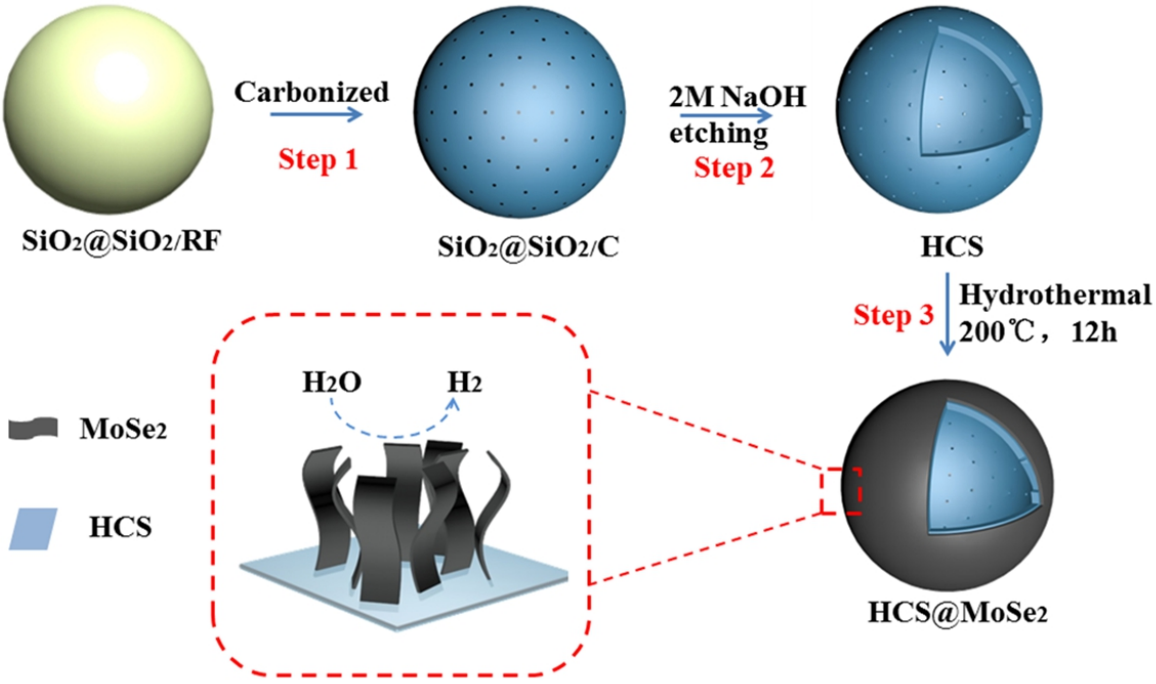


**Scheme 1** Schematic illustration of the synthesis of HCS@$MoSe_2$.

## 3. Results and Discussion

### 3.1. Synthesis and structural characterization

The preparation process of core-shell HCS@$MoSe_2$ hybrids is displayed in Scheme 1, which involves a three-step method. Firstly, the synthesized $SiO_2$@$SiO_2$/RF by modified Stober method[21] was carbonized by heating at 700 °C for 2 h under argon gas flow in a tube furnace leading to the formation of $SiO_2$@$SiO_2$/C. Secondly, the $SiO_2$ templates were removed by treating the material in 2 M sodium hydroxide for several hours and the HCS formed subsequently. Finally, ultrathin $MoSe_2$ nanosheets were grown on the HCS based via the hydrothermal treatment at 200 °C to form an HCS@$MoSe_2$ core-shell structure. Fig. 1a and 1b show the scanning electron micrograph (SEM) morphology of $SiO_2$@$SiO_2$/C and HCS, respectively. It can be seen that the $SiO_2$@$SiO_2$/C has a spherical morphology with a diameter of approximately 300 nm, and HCS obtained after etching of the $SiO_2$ keeps an initial structure of the template. It has been reported in the literature that there are abundant hydrophilic functional groups on the surface of HCS,[22] which indicated that HCS offer an attractive supporter for the attachment of $MoSe_2$ nanosheets. After the solvothermal process involving $NaMoO_4$ as the Mo source and Se powder as the Se source, the curly $MoSe_2$ nanosheets were uniformly decorated on the surface of the HCS (Fig. 1c), which is beneficial for the exposure of $MoSe_2$ active edges. In contrast, the pure $MoSe_2$ exhibited a pleated spherical configuration with an agglomerated structure (Fig. S1), indicating that the existence of HCS could avoid the stacking of $MoSe_2$ nanosheets. From Fig. 1d, it could be found that the petal-like $MoSe_2$ nanosheets were also inserted into the broken cavity of the hollow carbon framework. Moreover, the element mapping images in Fig. 1e show a homogeneous distribution of the Mo and Se elements on the surface of HCS. Similar hollow structure of HCS was also observed in transmission electron microscopy (TEM) images in Fig. 2a, and its outer shell layer is about 10 nm. In order to further confirm the structure of core-shell HCS@$MoSe_2$, the high resolution transmission electron microscopy (HRTEM) was carried out. As shown in Fig. 2c, d, the surface of core HCS was covered by a thin layer of $MoSe_2$ nanosheets without aggregation, and the interlayer spacing of 0.65 nm was in accordance with the (0 0 2) facet of $MoSe_2$. It is worth noting that the layered $MoSe_2$ nanosheets were composed of about 2-8 monolayers, which favor to expose more active sites and greatly enhance the HER catalytic performance.

Crystal structures of the as-synthesized core-shell HCS@$MoSe_2$, pure $MoSe_2$ and HCS were studied by XRD as shown in Fig. 3a. As for pure $MoSe_2$, the diffraction peaks at 2θ=13.7°, 27.6°, 34.4°, 41.9°, 47.5° and 56.9° can be respectively indexed to the (0 0 2), (0 0 4) (1 0 2), (0 0 6), (1 0 5) and (0 0 8) diffraction planes of the hexagonal 2H-$MoSe_2$ phase (JCPDS:29-0914), revealing the high purity of $MoSe_2$ nanosheets[23-24]. The XRD pattern of core-shell HCS@$MoSe_2$ hybrids show diffraction peaks corresponding with (0 0 2), (1 0 2), and (0 0 8) crystal facets of hexagonal 2H-$MoSe_2$ phase, indicating that the HCS were completely covered by the petal-like $MoSe_2$ nanosheets.

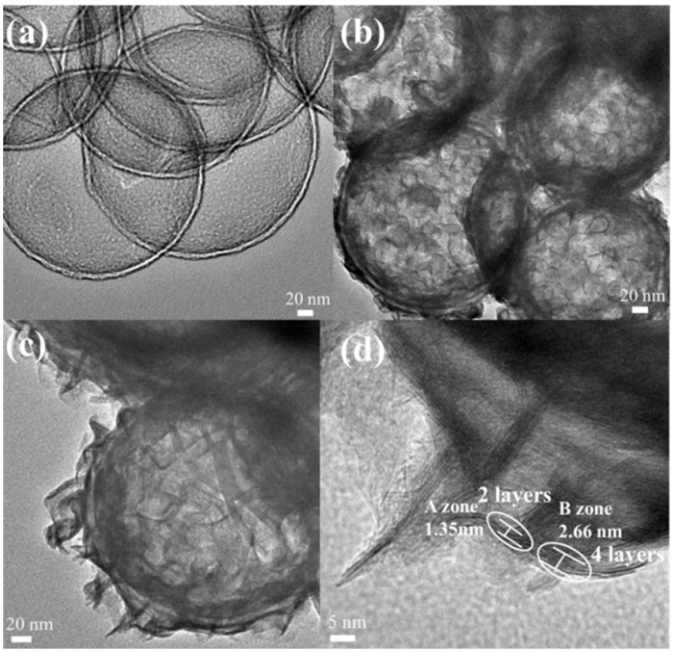


**Fig. 2** TEM images of (a) HCS and (b, c) HCS@$MoSe_2$; (d) HRTEM images of HCS@$MoSe_2$.

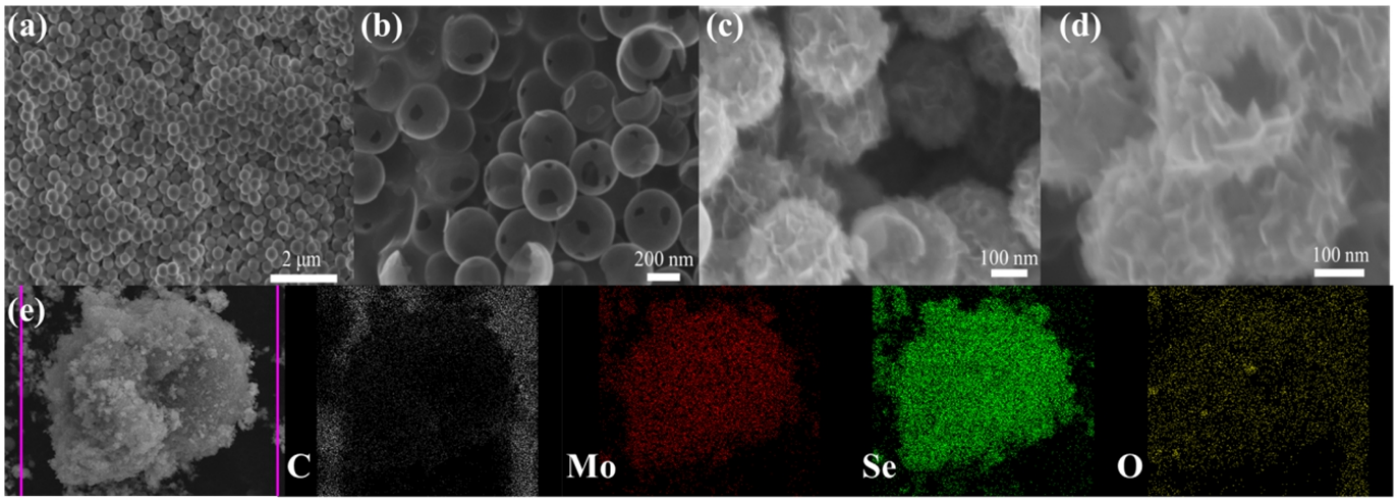


**Fig. 1** SEM images for the prepared (a) $SiO_2$@$SiO_2$/RF (b)HCS and (c,d) HCS@$MoSe_2$; (e) EDX mapping images (the element of C, Se, Mo) of HCS@$MoSe_2$ hybrids.

Raman spectroscopy was employed to further study the structure of the HCS@$MoSe_2$. The typical peaks of pure $MoSe_2$ at 238 and 281 $cm^{-1}$ can be observed in the spectra (Fig. 3b), which corresponds to the out-of-plane $A_{1g}$ mode and in-plane $E_{2g}^1$ mode of $MoSe_2$, respectively.[25] In addition, the D and G bands of the HCS were located at 1335 and 1591 $cm^{-1}$ respectively.[26] From the Raman spectrum of HCS@$MoSe_2$, the characteristic peaks corresponding to $MoSe_2$ nanosheet and the carbon D and G bands with the HCS were all observed, confirming the successful integration of the $MoSe_2$ nanosheets with HCS templates.

To reveal the interaction between $MoSe_2$ nanoparticles and HCS in the core-shell HCS@$MoSe_2$, the bonding characterization of the hybrids by ATR-FTIR analysis of HCS and HCS@$MoSe_2$ are shown in Fig. 3c. In the region of 750-2200 $cm^{-1}$, the strong absorption bands for HCS at 1670 and 1114 $cm^{-1}$ are ascribed to the C=O stretching vibrations of organic solutions and C-O(H) stretching vibrations peak, which exhibits the existence of the surface hydrophilic functional groups OH on the as-prepared HCS. Whereas the absorption bands at 897 $cm^{-1}$ and 790 $cm^{-1}$ can be assigned to C-C stretching and C-H bending modes, respectively. For the HCS@$MoSe_2$ hybrids, the characteristic absorption peaks are consistent with HCS except the C-O(H) stretching peak (1100 $cm^{-1}$) , which shows broadened and red-shifted feature obviously. This phenomenon implies the oxygen (O) in C-O is bonding to the metal molybdenum (Mo) in $MoSe_2$, making the interaction between carbon (C) in HCS and oxygen (O) in OH functional groups above mentioned become weaker, resulting in red-shift of C-O(H) stretching vibration. Correspondingly, it can be seen a new peak at 950 $cm^{-1}$ attributed to the formation of Mo-O bonds.[27] This formation of the surface hydrophilic functional groups on HCS is not only beneficial to the tight attachment of $MoSe_2$ nanosheets on HCS for stability, but also conducive to electronic transmission.

In order to further analyze the chemical composition and valence states of the HCS@$MoSe_2$, XPS spectrum was carried out in Fig. 4. The survey spectrum in Fig. 4a indicates the presence of Mo, Se, C, and O elements in the composite, which is in good agreement with the EDS results. C is originated from HCS core, and O is originated from the Mo-O bonds or partial surface oxidation of the $MoSe_2$ nanoparticles. The high resolution spectrum of C1s exhibits three peaks at 283.0 eV , 284.6 eV and 286.1 eV are ascribed to C-O, C-C and C-Mo

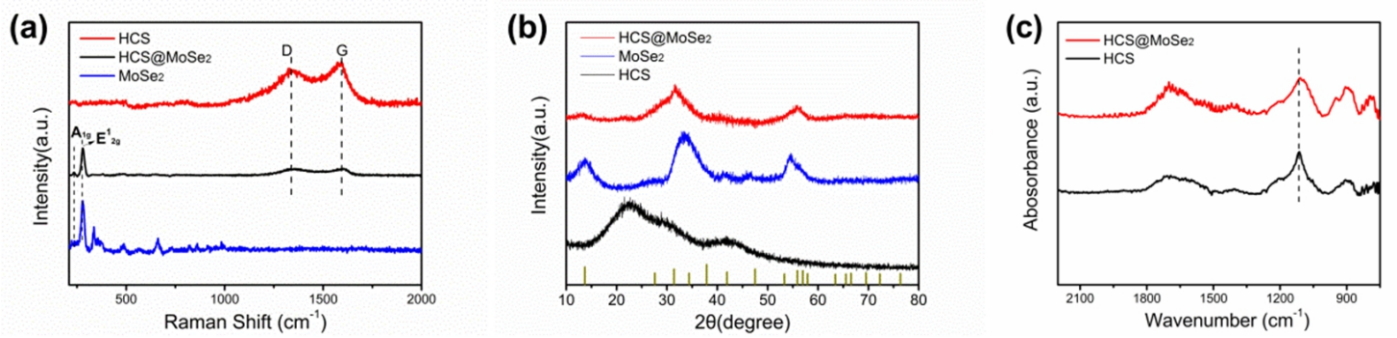


**Fig. 3** XRD patterns (a) and (b) Raman spectra of HCS, pure $MoSe_2$ nanosheets, and HCS@$MoSe_2$, (c)ATR-FTIR spectra of HCS and HCS@$MoSe_2$.

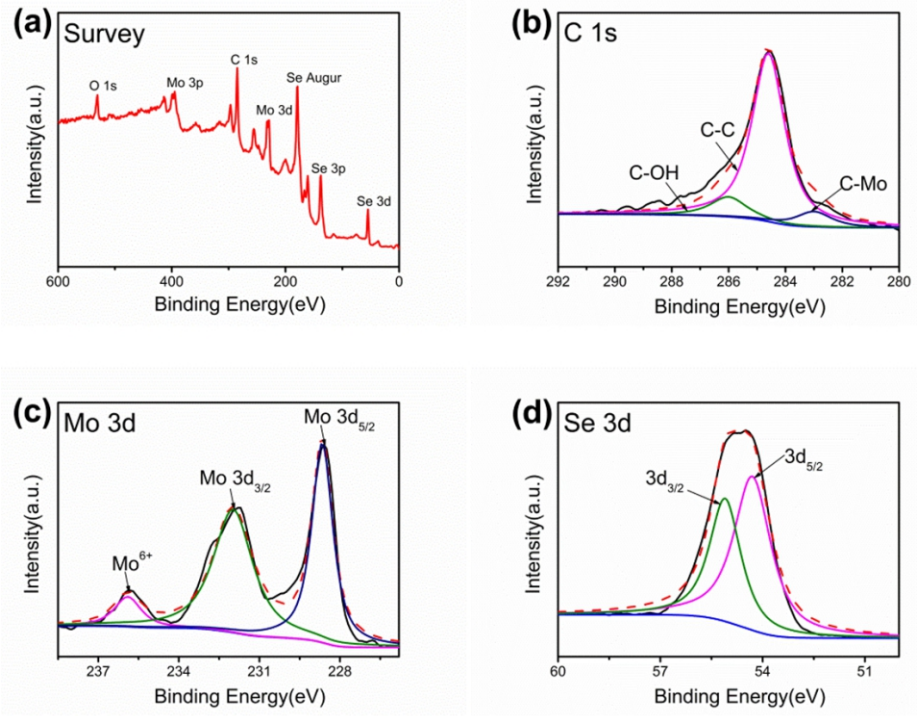


**Fig. 4** XPS spectra of HCS@$MoSe_2$ composite: (a) survey spectrum, (b) C 1s, (c) Mo 3d, (d) Se 3d.

respectively,[28] indicating the combination of HCS and $MoSe_2$ mainly depends on Mo-C and Mo-O bonding.[29] As depicted in Fig. 4c, two characteristic peaks located at 228.7 eV and 232.0 eV can be assigned to Mo $3d_{5/3}$ and Mo $3d_{2/3}$ spin orbit peaks of $MoSe_2$, which indicated that Mo is basically in the Mo (IV) state.[30] The small peak at 235.9 eV can be ascribed to $Mo^{6+}$ from $MoO_4^{2-}$. Meanwhile, the Se 3d can be deconvoluted into Se $3d_{5/2}$ and Se $3d_{3/2}$ at 54.3 eV and 55.1 eV, indicating the state of $Se^{2-}$.[31] Moreover, the detailed compositional analysis reveals that the surface Mo:Se atomic is 12.99 : 6.42, which is close to the formula of $MoSe_2$.

### 3.2. Electrocatalytic properties evaluation

The HER measurements of core-shell HCS@$MoSe_2$ hybrids, the pure $MoSe_2$ and HCS were performed in a three-electrode setup using a $H_2SO_4$ solution (0.5 M) at room temperature. In general, an ideal HER catalyst is capable of providing a high current at a low overpotential, along with a low onset potential. Firstly, the electrochemical activity of different materials was measured by LSV in Fig. 5a. As expected, the Pt/C (10 wt%) catalyst exhibited extremely high HER activity with a near zero onset potential and a large current density. On the contrary, the HCS have nothing to be with HER activity since there is almost no reduction current even at the electrode potential reaching to 0.35 V (vs. RHE). Pure $MoSe_2$ exhibited poor HER activity with the lower catalytic current and more negative onset potential due to its severe aggregation and low conductivity. The cathodic polarization curve of the HCS@$MoSe_2$ hybrids shows the best current density and exhibit a lower overpotential of 200 mV at a current density of 10 mA $cm^{-2}$, which is much smaller than that of pure $MoSe_2$ (10 mA $cm^{-2}$ at 300 mV) and better than reported $MoSe_2$ based electrocatalysts in acidic solution (Table 1).

The excellent performance of HCS@$MoSe_2$ hybrids from the uniformly distribution of $MoSe_2$ nanosheets on the surface of HCS, which exposes much more active edges and provides abundant catalytic sites for the HER process, thus leading to obtain optimized HER catalytic activity. The Tafel slope can be deduced from the Tafel equation:

$$\eta = b\log(j) + a$$

where $\eta$ is the overpotential, $j$ is the current density and b is the Tafel slope. The Tafel slope is always correlated with the reaction pathway and the adsorption type,[36] which reveals inherent property of catalyst materials and indicates the rate-determining step in the whole HER process. Besides, a small Tafel slope is preferred as it means a faster increase of hydrogen generation rate with increasing overpotential applied.[37] Tafel slopes for the HCS@$MoSe_2$ electrode was about 74 mV $dec^{-1}$, which was smaller than that of the pure $MoSe_2$ (100 mV $dec^{-1}$) in Fig. 5b, indicating that the HCS@$MoSe_2$ electrode has a faster kinetics of hydrogen generation. According to the mechanism of hydrogen evolution, the HER process mainly contains three possible elementary reactions in acidic medium. The Volmer reaction can also be called discharge reaction ($H^+ + e^- \rightarrow H_{ads}$), which usually has a high Tafel slope of 120 mV $dec^{-1}$; Heyrovsky reaction (electrochemical desorption): $H_{ads} + H^+ + e^- \rightarrow H_2$ and Tafel reaction (Recombination): $H_{ads} + H_{ads} \rightarrow H_2$ may also occur in the HER process, at which the Tafel slope value will be significantly reduced to 40 mV $dec^{-1}$ and 30 mV $dec^{-1}$ respectively.[38] Therefore, the HER process of the HCS@$MoSe_2$ electrode can be considered as the Volmer-Heyrovsky mechanism based on the principle of HER dynamics, and the Volmer reaction is used as the rate determining step.

Electrochemical impedance spectroscopy (EIS) is an important technique for studying the interfacial reaction and electron transfer kinetics. To understand the electrode kinetics during HER, the measurement was performed for HCS@$MoSe_2$ hybrids and pure $MoSe_2$. Fig. 5c displays the Nyquist plots of two catalysts and a facile Randle equivalent circuit is plotted in the inset to model the impedance data, in which the observed semicircle is primarily attributed to the charge transfer resistance ($R_{ct}$) of the $H^+$ reduction at the electrode-electrolyte interface. A lower $R_{ct}$ corresponds to a faster electron transfer. The $R_{ct}$ of HCS@$MoSe_2$ hybrids is about 8.9 Ω, which is remarkably reduced as compared to those of pure $MoSe_2$ (52 Ω). This demonstrates that HCS core dramatically enhance the electron transfer.

Electrochemical effective surface area (ECSA) is commonly used to evaluate the active sites of electrocatalysts. To further understand the enhanced catalytic activity of HCS@$MoSe_2$ hybrids, the double-layer capacity ($C_{dl}$) is measured by simple cyclic voltammetry (Fig. S3), which has been proved to be an effective parameter to estimate the electrochemically active surface area of the catalyst.[39] The positive and negative current density differences ($\Delta J = j_a - j_c$) are plotted at a given potential of 0.3V versus RHE against the scan rate, where half of the slope value is $C_{dl}$ in Fig. 5d. It is worth noting that the HCS@$MoSe_2$ hybrids (4.1 mF $cm^{-2}$) have almost twice the capacitance of pure $MoSe_2$ nanosheets (2.3 mF $cm^{-2}$), which means that the growth of $MoSe_2$ nanosheets uniformly on HCS can increase the number of active electrocatalytic sites and improve catalytic performance.

The durability is another major concern for an electrocatalyst. A potential long-term cycling is performed by taking continuous cyclic voltammograms (CVs) at a sweep rate of 0.1 V $s^{-1}$ for 1000 cycles from -0.34V to 0.06V (vs. RHE). The current density of the HCS@$MoSe_2$ hybrids decreased slightly compared with its initial state, demonstrating its good stability during long term cycling.

**Table 1.** Comparison of the HER activity of HCS@$MoSe_2$ with the reported $MoSe_2$ based electrocatalysts in acidic solution.

| Catalyst | Electrolyte Current density $j$ (mA $cm^{-2}$) | Corresponding overpotential (mV) | Refs. |
|---|---|---|---|
| $MoSe_x$/Mo | 10 | 270 | 32 |
| $MoS_{2(1-x)}Se_{2x}$ | 10 | 273 | 33 |
| $MoSe_2$/CC | 6 | 220 | 34 |
| $MoSe_2$ nanoflower | 10.96 | 300 | 35 |
| HCS@$MoSe_2$ | 10 | 200 | This work |

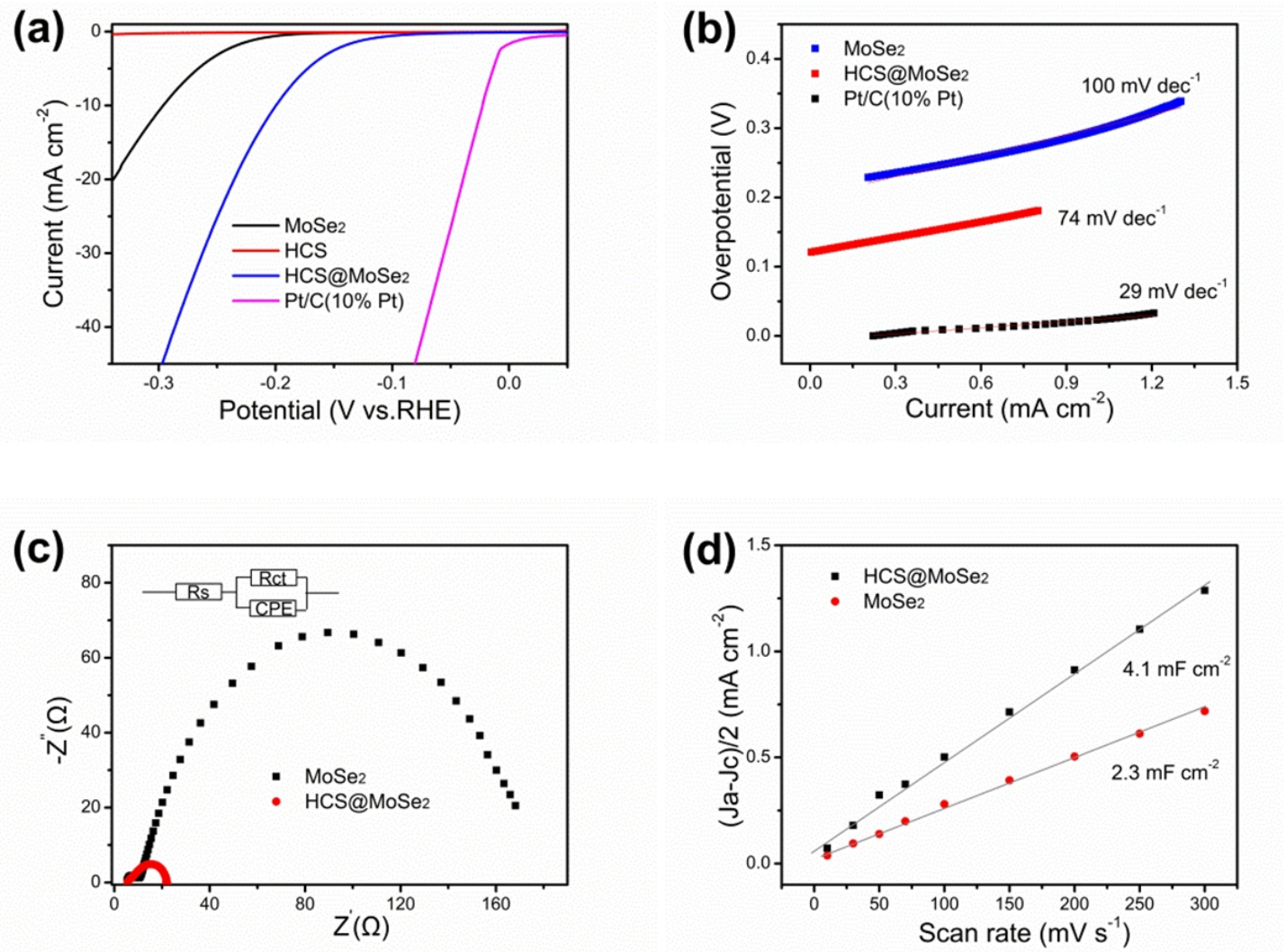


**Fig. 5** (a) LSV polarization curves for HCS, pure $MoSe_2$ nanosheets, and HCS@$MoSe_2$ hybrid modified GCE in 0.5 M $H_2SO_4$ solution. Scan rate: 5 mV $s^{-1}$; (b)The Tafel plots of the commercial Pt/C, pure $MoSe_2$ nanosheets and HCS@$MoSe_2$ respectively; (c)EIS Nyquist plots for pure $MoSe_2$ nanosheets and HCS@$MoSe_2$ modified electrodes; The inset shows the simplified Randles equivalent circuit; (d) Variation of double-layer charging currents at 0.3 V as a function of the voltage scan rate.

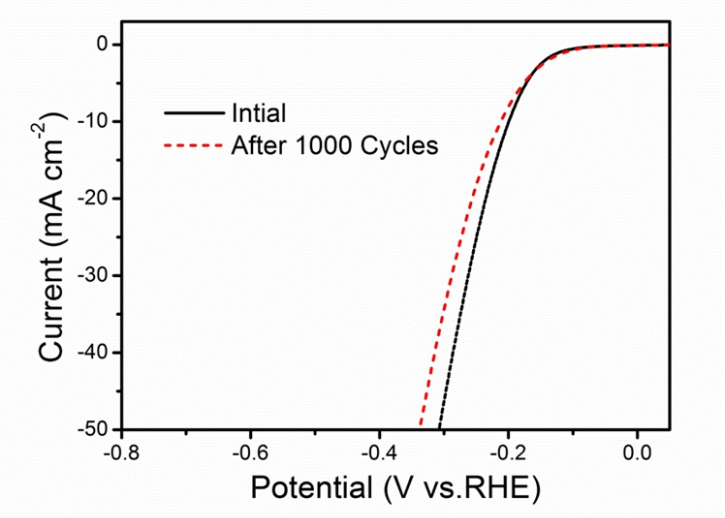


**Fig. 6** Stability test of the HCS@$MoSe_2$ composite.

## 4. Conclusions

In summary, the $MoSe_2$ nanosheets were successfully grown on HCS by a three-step method, which displayed a highly efficient HER performance. The $MoSe_2$ nanosheets were uniformly distributed on HCS which expose more active sites, and the HCS core provide a beneficial conductive environment for fast electron-transfer. When tested as electrode materials for HER, HCS@$MoSe_2$ have a small Tafel slope of 74 mV $dec^{-1}$, a small overpotential of 200 mV at a current density of 10 mA $cm^{-2}$, and a good long-term durability. Therefore, our research provides a promising pathway for synthesis of efficient electrocatalysts, which have the potential to replace Pt-based catalysts.

## Supporting Information

Additional Figs. S1-S3.

## Acknowledgements

The authors gratefully acknowledge the financial support offered by NSFC Grants (21373152).

## References


1. Q. H. Wang, K. Kalantar-Zadeh, A. Kis, J. N. Coleman and M. S. Strano, *Nat. Nanotechnol*., 2012, **7**, 699-712.
2. M. Xu, T. Liang, M. Shi and H. Chen, *Chem. Rev*., 2013, **113**, 3766-3798.
3. J. Xie, H. Zhang, S. Li, R. Wang, X. Sun, M. Zhou and J. Zhou, et al., *Adv. Mater*., 2013, **25**, 5807-5813.
4. J. Xie, J. Zhang, S. Li, F. Grote, X. Zhang, H. Zhang, R. Wang, Y. Lei, B. Pan and Y. Xie, *J. Am. Chem. Soc*., 2013, **135**, 17881-17888.
5. H. Shu, D. Zhou, F. Li, D. Cao and X. Chen, *ACS Appl. Mater. Interfaces*, 2017, **9**, 42688-42698.
6. J. Kibsgaard, Z. Chen, B. N. Reinecke and T. F. Jaramillo, *Nat. Mater*., 2012, **11**, 963-969.
7. D. Kong, H. Wang, J. J. Cha, M. Pasta, K. J. Koski, J. Yao and Y. Cui, *Nano Lett.*, 2013, **13**, 1341-1347.
8. X. Zhou, J. Jiang, T. Ding, J. Zhang, B. Pan, J. Zuo and Q. Yang, *Nanoscale*, 2014, **6**, 11046-11051.
9. X. Y. Yu, H. Hu, Y. Wang, H. Chen and X.W.D. Lou, *Angew. Chem. Int. Ed.*, 2015, **54**, 7395-7398.
10. Y. Huang, H. Lu, H. Gu, J. Fu, S. Mo, C. Wei, Y. E. Miao and T. Liu, *Nanoscale*, 2015, **7**, 18595-18602.
11. C. Xu, S. Peng, C. Tan, H. Ang, H. Tan, H. Zhang and Q. Yan, *J. Mater. Chem. A*, 2014, **2**, 5597-5601.
12. R. J. Wang, P. Sun, H. W. Wang and X. F. Wang, *Electrochim. Acta*, 2017, **258**, 876-882.
13. F. Lai, D. Yong, X. Ning, B. Pan, Y. E. Miao and T. Liu, *Small*, 2017, **13**, 1602866.
14. L. Jia, X. Sun, Y. Jiang, S. Yu and C. Wang, *Adv. Funct. Mater*., 2015, **25**, 1814-1820.
15. S. Deng, Y. Zhong, Y. Zeng, Y. Wang, Z. Yao, F. Yang, S. Lin, X. Wang, X. Lu, X. Xia and J. Tu, *Adv. Mater*., 2017, **29**, 1700748.
16. S. B. Yang, X. L. Feng, L. J. Zhi, Q. A. Cao, J. Maier and K. Müllen, *Adv. Mater.*, 2010, **22**, 838-842.
17. K. X. Wang, Z. L. Li, Y. G. Wang, H. M. Liu, J. S. Chen, J. Holmes and H. S. Zhou, *J. Mater. Chem*., 2010, **20**, 9748-9753.
18. S. Yoon and A. Manthiram , *J. Phys. Chem. C,* 2011, **115**, 9410-9416.
19. K. Tang, R. J. White, X. Mu, M. M. Titirici, P. van Aken and J. Maier, *ChemSusChem,* 2012, **5**, 400-403.
20. L. Zhang and X. W. Lou, *Chem.*, 2014, **20**, 5219-5223.
21. W. S. A. F. E. Bohn, *J. Colloid Interface Sci*., 1968, **26**, 62-69.
22. J. Liu, S. Z. Qiao, H. Liu, J. Chen, A. Orpe, D. Zhao and G. Q. M. Lu, *Angew. Chem. Int. Ed.*, 2011, **50**, 5947-5951.
23. W. Guo, Y. Chen, L. Wang, J. Xu, D. Zeng and D. L. Peng, *Electrochim. Acta*, 2017, **231**, 69-76.
24. O. E. Meiron, V. Kuraganti, I. Hod, R. Bar-Ziv and M. Bar-Sadan, *Nanoscale*, 2017, **9**, 13998-14005.
25. T. X. Thai, S. Poorahong and M. Siaj, *RSC Adv*., 2017, **7**, 52345-52351.
26. X. Y. Li, Q. G. Xiao, Y. Y. Gao, H. L. Zhang, H. B. Xu and Y. Zhang, *J. Alloys Compd*., 2017, **723** ,1113-1120.
27. W.G. Klemperer, V. V. Mainz, R. C. Wang and W. Shum, *Inorg. Chem*., 1985, **24**, 1968-1970.
28. Y. Liu, M. Zhu and D. Chen, *J. Mater. Chem. A*, 2015, **3**, 11857-11862.
29. X. Zhao, W. Cai, Y. Yang, X. Song, Z. Neale, H. E. Wang, J. Sui and G. Cao, *Nano Energy*, 2018, **47**, 224-234.
30. C. Dai, Z. Zhou, C. Tian, Y. Li, C. Yang, X. Gao and X. Tian, *J. Phys. Chem. C*, 2017, **121**, 1974-1981.
31. B. Qu, C. Li, C. Zhu, S. Wang, X. Zhang and Y. Chen, *Nanoscale*, 2016, **8**, 16886-16893.
32. S. N. Grigoriev, V. Y. Fominski, R. I. Romanov, M. A.Volosova and A. V. Shelyakov, *Thin Solid Films*, 2015, **592**, 175-181;
33. L. F. Yang, F. Lei , Q. Wang and W. H. Huang, *Nanoscale*, 2015, **7**, 10490-10497.
34. Y. D. Liu, L. Zhang, Q. Zhen, X. Li and H. X. Zhong, *Sci. Rep*., 2016, **6**, 22516;
35. Ravikumar, H. Chandan, Nair, G. Vishnu, H. Balakrishna and R. Geetha, *Mater. Lett*., 2018, **220**, 133-135.
36. Y. Chen, K. Yang, B. Jiang, J. Li, M. Zeng and L. Fu, *J. Mater. Chem. A*, 2017, **5**, 8187-8208.
37. Y. Li, H. Wang, L. Xie, Y. Liang, G. Hong and H. Dai, *J. Am. Chem. Soc*., 2011, **133**, 7296-7299.
38. X. Zou and Y. Zhang, *Chem. Soc. Rev*., 2015, **44**, 5148-5180.
39. C. Jian, Q. Cai, W. Hong, J. Li and W. Liu, *Small*, 2018, **17**, 1703798.